UC Davis
UC Davis Previously Published Works

Title

Cone beam CT multisource configurations: evaluating image quality, scatter, and dose using phantom imaging and Monte Carlo simulations

Permalink

https://escholarship.org/uc/item/4m39p2xf

Journal

Physics in Medicine and Biology, 65(23)

ISSN

0031-9155

Authors

Becker, Amy E
Hernandez, Andrew M
Schwoebel, Paul R
et al.

Publication Date

2020-12-07

DOI

10.1088/1361-6560/abc306

Peer reviewed

Cone beam CT multisource configurations: evaluating image quality, scatter, and dose using phantom imaging and Monte Carlo simulations

Amy E Becker[1], **Andrew M Hernandez**[2], **Paul R Schwoebel**[3,4], **John M Boone**[1,2]

[1]Department of Biomedical Engineering, University of California Davis, Sacramento, CA 95817, United States of America

[2]Department of Radiology, University of California Davis, Sacramento, CA 95817, United States of America

[3]Department of Physics, University of New Mexico, Albuquerque, NM 87131, United States of America

[4]SRI International, Applied Physics, Menlo Park, CA 94025, United States of America

Abstract

The purpose of this study was to compare various multisource configurations applied to cone beam CT (CBCT) using phantom imaging and Monte Carlo simulations. Image quality, scatter, and dose were evaluated in both overlapping (large cone angle) and collimated (small cone angle) configurations for CBCT. Four x-ray tube configurations were considered: traditional one source, three source overlapping, six source overlapping, and six source collimated. Image quality was evaluated on a prototype breast CT system using the following five phantoms: a Defrise phantom, a previously reported CBCT QA phantom (Corgi), a polyethylene cylinder, and two anthropomorphic phantoms (hand and knee). Scatter contamination and radiation dose were evaluated using Monte Carlo simulations of a voxelized polyethylene cylinder. The modulation of the Defrise phantom disks on average was 2.7X greater for the six source collimated configuration than the six source overlapping configuration. The data lost from cone beam artifact (spatial domain) and the null cone (frequency domain) in the overlapping configuration were completely recovered using the collimated configuration. The maximum scatter-to-primary ratio (SPR) for the overlapping configuration was 0.81 and the maximum SPR for the collimated configuration was 0.26. The average dose and maximum dose was 4X less in the collimated six source configuration when compared with the overlapping configurations. The maximum dose for the overlapping configurations (one, three & six) remained constant, but the average dose for the multisource (three & six source) overlapping configurations increased 25% when compared to the one source configuration. Use of a collimated multisource x-ray tube configuration was shown to provide significant improvements in image quality throughout the cone-beam geometry field-of-view, reduction in scatter contamination, and more efficient use of dose in comparison to both the traditional CBCT geometry with a single source and the overlapping multisource configurations.

xrayimagingamy@gmail.com .

Keywords

cone beam artifact; x-ray scatter; image quality; computed tomography

1. Introduction

Cone beam CT (CBCT) was originally developed in 1982 for angiography (Robb 1982), but it was not until the late 1990s that advancements in flat panel detectors (FPD) and computer technology made it possible to produce CBCT systems for routine clinical use. In the last 20 years, clinical use and continued research in CBCT has expanded its application to include angiography (Fahrig *et al* 2006), oral and maxillofacial imaging (Miracle and Mukherji 2009), interventional radiology (Jaffray *et al* 2008), image guided radiotheraphy (Jaffray *et al* 2002), musculoskeletal imaging (Posadzy *et al* 2018) and breast imaging (Lindfors *et al* 2008, Gazi *et al* 2015). The main benefits of CBCT over traditional multi-detector CT (MDCT) are higher spatial resolution with reduced cost, dose, and space requirements (Posadzy *et al* 2018). This has greatly increased accessibility to CT imaging for both researchers and clinicians and has allowed unique geometries to be designed for specialized applications. Conventional CBCT scanners expose the patient extremity with a cone shaped x-ray beam that covers the entire object. Projection data is collected on a FPD with a typically circular trajectory and that data is reconstructed into a 3D volume dataset.

There are known general disadvantages of CBCT that need to be better investigated to ensure that image quality and clinical outcomes are not compromised when switching from MDCT to CBCT. First, the common circular trajectory of the source is a known limitation because it does not meet the Kirillov–Tuy condition (Tuy 1983) for complete 3D image reconstruction—leading to inherent cone beam artifacts along the z-axis and incomplete sampling in the Fourier domain. These artifacts are most pronounced at large cone angles resulting in inconsistent image quality (Ozaki *et al* 2013) throughout the field of view (FOV) which can reduce the diagnostic quality and quantitative integrity of CBCT when compared to MDCT. A second limitation of CBCT is the size of the object that can be scanned, since the maximum object FOV is smaller in CBCT than MDCT. Another limitation for CBCT applications in image guided therapy is that the planning target volumes often require multiple scans to cover the entire area of interest, which extends the total scan time. CBCT also suffers more from scatter than MDCT, due to the larger x-ray beam field size, and this increases noise and decreases contrast resolution (Endo *et al* 2001, Scarfe and Farman 2008).

A common problem with traditional CBCT reported in clinical comparisons between MDCT vs. CBCT was the inconsistency in image quality throughout the FOV (i.e. better image quality near the central ray and worse toward the periphery of the FOV) generally caused by scatter, noise, and artifacts. Several groups have made direct comparisons between CBCT vs. MDCT for clinically relevant tasks and these studies reveal the limitations of current CBCT for various clinical applications.

For image guided radiotherapy, the limited FOV and inaccurate Hounsfield Unit values of CBCT were shown to cause inaccuracies in treatment planning when compared to

MDCT in both phantom and patient cases (Yoo and Yin 2006). For the characterization of musculoskeletal trauma in cadaver knees and hands, it was shown that MDCT was favorable to CBCT by radiologists for soft tissue tasks (Demehri *et al* 2015). In a large cohort patient study (Faccioli *et al* 2010) comparing MDCT to CBCT, post-traumatic finger fractures were missed in CBCT. Another study that compared the application of MDCT and CBCT in cadaver wrists found that CBCT was less sensitive than MDCT at detecting fractures (Neubauer *et al* 2016). CBCT applied to orthodontics in cadaver studies was shown to result in large and frequently inaccurate bone height measurements when compared to physical measurements (Wood *et al* 2013) and was also shown to be less accurate than MDCT for bone density evaluation (Parsa *et al* 2015).

There have been efforts to overcome the undersampling problem in CBCT, with multisource x-ray source configurations (Gang *et al* 2018), computer simulations of inverse CBCT systems (Schmidt *et al* 2004, Gilat Schmidt 2009), prototype development of inverse CT systems (Neculaes *et al* 2016), and development of correction techniques in the image reconstruction algorithm (Baek and Pelc 2010, Han and Baek 2019). Complex geometries (e.g. helical, saddle, line and circle) aim to meet the Kirillov–Tuy condition (Tuy 1983), but at the expense of complicated hardware and mechanical alignment systems. Multiple individual x-ray sources have been applied to CBCT and have shown improvements in the reduction of cone beam artifacts with a physical prototype (Gang *et al* 2018), but still suffer from photon scatter caused by large field sizes. Numerical simulations have been used to study multiple parallel circular cone beam orbits (Zhye and De Man Bruno 2009, Fu and Fan 2015), the saddle geometry (Shah *et al* 2015), the line and circle geometry (Vedantham *et al* 2012), multithreaded cardiac CT (Kachelrieß *et al* 2006), helical CBCT (Zhao *et al* 2009), semi-stationary CT (Chen *et al* 2014a) and stationary CT (Chen *et al* 2014b). Current methods for scatter correction in CBCT include physical collimators and anti-scatter grids (Siewerdsen *et al* 2004), as well as software correction algorithms based on Monte Carlo estimation (Poludniowski *et al* 2009, Chen *et al* 2016), physical measurements (Siewerdsen *et al* 2005, Zhu *et al* 2009, Gong *et al* 2018) or postprocessing in the image domain (Ghazi *et al* 2019).

The present study will preserve the simplicity of the circular trajectory in CBCT with analytical image reconstruction while overcoming the limitations of cone beam artifacts and scatter caused by large field sizes, extending the FOV, and distributing the dose more effectively. This solution could offer improved image quality in the many applications that suffer from artifacts caused by the non-ideal geometry in conventional CBCT.

Physical experiments were performed to evaluate image quality using a prototype CBCT system and Monte Carlo simulations were applied to evaluate both the 3D dose distribution in a voxelized polyethylene phantom and scatter contributions in the projection domain for various multisource configurations. Three multisource geometries were considered with two different collimation schemes. Traditional CBCT collimates the x-ray beam to cover the entire detector at once, and when applied for multisource techniques this will be referred to as the *overlapping* multisource geometry. We also consider a different approach to achieving full detector coverage in CBCT by stacking several small cone angle exposures, which will

be referred to as the *collimated* multisource geometry. The FOV for the reconstructed image domain remains the same across the comparisons.

2. Methods

2.1. Source configuration concept

Diagrams in figure 1 show the x-ray source positions and corresponding FOV sizes for the different source configurations considered in this study. Three multisource geometries were considered with two different collimation schemes. The CBCT collimation scheme that covers the entire detector at once will be referred to as the *overlapping* multisource geometry (figures 1(b) and (c)). We also consider a different collimation scheme by stacking several contiguous small cone angle acquisitions, which will be referred to as the *collimated* multisource geometry (figure 1(d)). In this study, six source locations with 30 mm separation between each source were simulated in both the overlapping and collimated geometry. Each vertical source position is assigned a letter (A–F) and those positions were constant across all geometries and experiments. Comparisons were made between the four different CBCT source configurations: (i) a one source, (ii) overlapping three source, (iii) overlapping six source, and (iv) collimated six source.

The ideal collimation system is depicted in figure 1, where the sources are uniquely collimated to cover the FOV with adjusted posterior and anterior cone angles. For the three source overlapping configuration (figure 1(b)) the cone angle of position A is 2° posteriorly and 14° anteriorly, for position C the cone angles are 6.9° posteriorly and 9.3° anteriorly, and for position E the cone angles are 11.7° posteriorly and 4.5° anteriorly. Similarly, for the six source overlapping geometry the cone angles of position A are 2°/14° (anterior/posterior), position B cone angles are 4.5°/11.7°, position C are 6.9°/9.3°, position D are 9.3°/6.9°, position E are 11.7°/4.5°, and position F are 14°/2°. This ideal collimation scheme was applied in the Monte Carlo simulations explained in section 2.3. However, the physical experiments (detailed in section 2.2) utilize a rigid collimation system (i.e. 2° posteriorly and 14° anteriorly) which cannot be adjusted and was predetermined by the built in x-ray tube housing. For the collimated system geometry, additional collimation was added anteriorly resulting in a 2° cone angle both posteriorly and anteriorly (figure 1(d)) and consistent for both the physical experiments and the Monte Carlo simulations.

2.2. Experimental study of CBCT system source configurations

2.2.1. CBCT system parameters—To illustrate various x-ray source configurations in CBCT, phantom imaging was performed on a prototype breast CBCT system 'Doheny' built at UC Davis. The relevant parameters are described here, but the complete system parameters are reported elsewhere (Gazi *et al* 2015). Doheny was designed as an approximate half cone system rather than a full cone system in order to maximize chest wall coverage for imaging the breast in the pendant geometry. The central ray is positioned near the chest wall with a maximum fan angle of 23.8°. Multiple scans using a one source x-ray tube were used to simulate a multiple-source CBCT system. A vertical actuator controlled by a stepping motor was used to move the one source x-ray tube to different vertical positions between scans and a full 360° CT acquisition was acquired at each position. A

full set of projection data were acquired producing 500 projections at each of the source positions (A–F as shown in figure 1). Individual projections were subsequently interleaved during image reconstruction to simulate a multisource x-ray tube system as detailed in section 2.2.2. All scans in this study were acquired at 60 kV with 0.2 mm Cu filtration, 150 mA, an x-ray pulse width of 4 milliseconds (ms), and a pulse period of 23 ms. The total tube current time product was therefore 180 mAs.

2.2.2.   Image reconstruction—The volume datasets were reconstructed using the Feldkamp-Davis-Kress (FDK) (Feldkamp *et al* 1984) 3D filtered back projection with a Shepp Logan apodization filter which was implemented in MATLAB using voxel-based back projection. Each volume data set was reconstructed using an isotropic voxel size of 150 μm and a matrix size of $1024 \times 1024 \times 1200$ voxels which creates a FOV of $150 \times 150 \times 180$ mm. In a previous study conducted on this system (Gazi *et al* 2015), the system modulation transfer function (MTF) was measured and the 10% MTF resolution limit was determined to be 3.33 mm^{-1}, which corresponds to a voxel size of 150 μm.

For all overlapping multisource geometries, the total tube time current product used to generate each reconstructed volume dataset was kept the same by interleaving a total of 500 projections. This was achieved by interleaving a subset of the original projections from each source, demonstrated in figure 2. Due to the built-in collimation of the x-ray tube housing, some of the projection data was lost when the x-ray source was moved from the original 'A' position. This was accounted for by linearly scaling each voxel value after reconstruction based on how many sources contributed to it. Rigid registration was applied for the overlapping multisource geometries.

For the collimated six-source multisource geometry, a narrow collimator was applied to limit the x-ray beam to a smaller region in the *z*-dimension for each source position (see figure 1(d)) and all 500 projections from each acquisition were used in the image reconstruction. These volumes were reconstructed into sub-volumes using the same FDK method as the one source configuration and all sub-volumes were combined in the CT image domain to complete the image reconstruction. Figure 3 shows the regions that were used in the collimated six-source multisource reconstruction, although the physical collimation is slightly larger than that in the diagram. In a fully assembled system, the collimation for each source would be designed precisely for the region on the detector used in the reconstruction. The coverage is contained within 1330 detector element 'dexel' rows resulting in 20 cm of vertical detector coverage from the inherent collimation on the system. These exact rows were not optimized for this preliminary study. The same total region on the detector (i.e. 20 cm vertical detector coverage) was used for the one source and the overlapping multisource configuration reconstruction.

2.2.3.   Defrise phantom—In order to demonstrate cone beam artifacts in the experimental studies on the Doheny scanner, a Defrise phantom (figure 4(a)) was built from evenly-spaced compact disks. The phantom is composed of 120 mm diameter polycarbonate disks 1.2 mm thick and evenly spaced using nylon plastic disks which are 25 mm in diameter and 2.4 mm thick. The overall height of the stack was 150 mm which is large enough to fill the entire object space. All four source configurations were used to image the

Defrise phantom and compare line profiles through the 3D reconstructions. The modulation of the Defrise disks was determined by finding the difference between the maximum (95th percentile) and minimum (5th percentile) within the line profile data.

2.2.4. Corgi phantom—A multi-purpose and modular quality assurance phantom (Siewerdsen *et al* 2019) for CBCT scanners was recently developed and commercialized, referred to as the Corgi phantom (figure 4(b)). Contained within this phantom is a cone beam artifact module consisting of Teflon disk pairs separated with polyethylene terephthalate and positioned vertically in the phantom at different cone angles. The diameter of each disk is 25.4 mm with a thickness of 1.0 mm, and the disks are spaced 3.0 mm apart vertically. For these experiments, four cone beam modules were positioned 30 mm from each other vertically within the phantom and used to quantify the magnitude of the z-axis modulation at these four regions of the reconstructed FOV. The modules were positioned vertically from the one source central ray location at 30 mm, 60 mm, 90 mm, and 120 mm to isolate specific cone angles within the scanner FOV. A metric (Siewerdsen *et al* 2019) has been developed for evaluating the magnitude of the cone beam artifact referred to as the z-modulation [z_{mod}] which is illustrated in figure 4(c) and defined in equation (1).

$$z_{mod} = \frac{\mu_t - \mu_m}{\mu_t - \mu_o}$$

(1)

where the mean reconstructed voxel value (μ, linear attenuation coefficient) is measured in the Teflon (t) disk, in the middle (m) region between the two Teflon disks, and the outside (o) region beyond the disks as depicted in figure 4. When the module is completely resolvable, the [z_{mod}] will approach unity and when it is completely unresolvable, the [z_{mod}] will be nearly zero. To calculate the μ_t, μ_m, and μ_o values, an ROI (9 mm × 9 mm) was averaged within each coronal slice to reduce noise in the estimation.

2.2.5. Noise power spectra—It is well known in CBCT that the 3D noise power spectrum (NPS) has a null cone (Bartolac *et al* 2009, Baek and Pelc 2011) that corresponds to the frequencies missing in the data and the cone angle used in the scan. This missing cone can be explained by the central slice theorem. For a single projection, the diverging rays in a cone beam tilt the 2D Fourier plane in the projection domain, which tilts the 3D Fourier plane in the reconstructed domain. Since all the projections are summed into the reconstruction, the many tilted 2D Fourier planes result in a cone shape in the reconstructed 3D Fourier domain. To characterize the noise properties and quantify the null cone, the 3D NPS was measured for the one source, three source, and six source configurations. Two identical scans of a polyethylene cylinder were reconstructed, and the data sets were subtracted to obtain a single noise-only image. The 3D *NPS*(u, v, w) was then calculated using the noise-only image with 100 overlapping volumes of interest (VOI) centered around a circle at half the radial distance of the polyethylene cylinder. A cylinder with a diameter of 154.2 mm was used in the acquisition, so the center of the VOIs were located at 38.1 mm from the isocenter and each volume was 128 × 128 × 128 voxels.

$$NPS(u, v, w) = \frac{1}{N} \sum_{i=1}^{N} \frac{|DFT_{3D}(VOI_i(x, y, z))|^2}{2} \frac{\Delta x}{N_x} \frac{\Delta y}{N_y} \frac{\Delta z}{N_z}.$$ (2)

In equation (2), the 3D frequency domain is represented by variables (u, v, w) and the corresponding 3D spatial domain is represented by variables (x, y, z). The VOI_i term is the individual cube of data within the difference data and the N term refers of the number of VOIs, which in this case is 100. The VOIs are 3D discrete Fourier transformed (DFT_{3D}), magnitude squared, and divided by two to account for the doubling of the noise magnitude during the subtraction step. The data from 100 VOIs were averaged and then scaled by the number [N_x, N_y, N_z] and size [Δx, Δy, Δz] of the voxels.

In order to quantify the null cone of the 3D NPS, the elements that were less than 10% of the 95th percentile of the entire 3D NPS were classified as the null elements (Gang *et al* 2018). This criterion was used to determine the null elements within the 3D NPS and the fraction of the total that were null for each multisource configuration. The percent null elements were plotted with respect to the z-dimension relative to the central ray for 16 regions down the length of the data. This was done in the same regions for the one source, overlapping multisource, and collimated multisource configurations.

2.3. Monte Carlo simulation of CBCT system source configurations

2.3.1. Simulation model—A validated Monte Carlo-based radiation transport code (MCNP X 2003) (MCNP6 version 1.0) was employed in this study to simulate: (1) primary and scatter contributions to projection images, and (2) 3D dose distributions for the various source configurations. For all simulations a 60 kV polyenergetic source with 0.2 mm Cu filtration was modeled using TASMICS (Hernandez and Boone 2014) and implemented in MCNP6 as a probability density function for the photon source distribution. The source was defined as a point with photon emission directed towards a simulated collimation window for either the overlapping or collimated geometry as shown in figure 1 and detailed in section 2.1. A phase space file was recorded for all photons passing through the collimator window using the source surface write card in MCNP which records each photon energy, direction, and location. The phase space files were then used with the source surface read card in MCNP to define the source for subsequent simulations detailed in the following two sections. A separate phase space file was recorded for all six sources in the overlapping geometry. Given the symmetric collimation (in z) for the collimated geometry, only a single-phase space file was generated and then translated (using the TR card in MCNP) in z to simulate all six sources. A 154.2 mm diameter polyethylene cylinder was modelled as a voxelized phantom 40 cm in length with an isotropic voxel size of 0.12 mm and centered about the scanner isocenter in x-y and the center of the detector FOV in z. This cylinder diameter matches that used in the NPS measurements in the experimental study. The excess phantom length beyond the 14.4 cm detector FOV was simulated in order to include the effects of backscatter.

For normalization of the projection image and dose simulations, the air kerma free-in-air was simulated at the isocenter by modelling a 0.6 cm^3 thimble ionization chamber (10×6–

0.6CT, RadCal Corp., Monrovia, CA, USA). A total of 6.0×10^8 and 1.3×10^9 photons were tracked and written to the phase space files for the collimated and overlapping geometry, respectively. This number of source photons was sufficient to ensure that the relative error was less than 1% across all projection, dose and air kerma simulations.

2.3.2.   Primary and scatter contributions to projection images—For simulation of projection images, the detector geometry detailed in section 2.2 was modeled in MCNP6. An ideal energy integrating detector model was implemented in the simulations which assumes 100% absorption efficiency of photons independent of detector material and incident angle (Smans *et al* 2010). The estimated scatter-to-primary ratio (SPR) from this model is within ~5% of measured values for the photon energy range investigated in this work providing confidence that this detector model is suitable for the purpose of this work. Simulation of the native dexel pitch (0.075 mm) for the FPD utilized in this work is superfluous for the purpose of comparing the primary and scatter contributions across the different source configurations. Moreover, the scatter contribution to projection images is a relatively low frequency effect and does not require high resolution simulations for accurate estimation. Therefore, the primary projection images were simulated with a dexel pitch of 0.75 mm using a grid of point detector tallies (*F5 in MCNP6), after correcting for the surface area of each dexel and the cosine of the angle between the primary x-rays and the normal to the detector surface (Smans *et al* 2010). The scatter projection images were simulated with a dexel pitch of 3.75 mm using a grid of *F1 tallies which records the energy current through the detector surface using a modification card to discriminate between primary and scatter contributions. Lastly, the low-resolution scatter projections were interpolated to match the resolution of the primary projections and then used to calculate the SPR across the entire detector surface. The primary, scatter, and SPR projections were compared across the different source configurations investigated in this work. The simulated air kerma (mGy per source particle) was scaled to the detector surface using the inverse square law and used to normalize all projection images (MeV per source particle) such that each dexel is in units of MeV per mGy at the detector surface.

2.3.3.   3D dose distributions—The energy deposited per unit mass (MeV g^{-1}) was estimated for each voxel within the voxelized polyethylene phantom using the F6 tally in MCNP6 and converted to units of dose (mGy) by multiplying the tally output by 1.6022 $\times 10^{-7}$. 3D dose distributions were simulated for all six sources in both the collimated and overlapping geometry (12 total simulations). All dose distributions were then divided by the simulated air kerma at the isocenter such that the unit of each voxel is absorbed dose per air kerma (mGy mGy^{-1}). Given that the cylindrical phantom is homogenous and symmetric about the scanner isocenter, separate simulations were not required for rotating the phantom (or source). Phantom rotation was accomplished by bilinear interpolation of the 3D dose distribution for a single projection through any arbitrary rotation angle, ensuring that the rotated dose map was the same size as the original dose map. This approach to estimating the dose distribution for an entire CBCT scan allows for flexibility in simulating any arbitrary number of rotation angles, orbital extent, source configuration, and source exposure sequencing.

2.4. Anthropomorphic phantom imaging

An anthropomorphic hand phantom measuring 25 mm × 110 mm × 200 mm and an anthropomorphic knee phantom measuring 150 mm × 150 mm × 250 mm were scanned to show the subjective differences in image quality for two simple clinical imaging tasks. The same scan protocol that was previously described was applied using the one source configuration and the collimated six source configuration.

3. Results

3.1. Experimental study of CBCT system source configurations

3.1.1. Defrise phantom—The results from the Defrise phantom for the various source configurations are shown in figure 5. A single sagittal slice through the center of the reconstructed volume data set shows qualitative differences between the source configurations. An arrow is superimposed onto each image to show where data was extracted for a line plot from the top to bottom slices. Line plots were created to quantify the cone beam artifacts. A region of 2 × 2 pixels in the coronal plane was averaged for each slice of the line plot to reduce noise. When the one source configuration was used to image the Defrise phantom, the disks are distinguishable for only a small region of the total FOV, about 30 mm in the vertical direction near the central ray of the x-ray beam. The same trend is apparent in the three-source overlapping configuration, where the visibility of the disks is improved near each of the central rays of the x-ray beam. The six-source overlapping configuration resolves the disks for the entire phantom, however a considerable fraction of the modulation intensity is lost. The modulation of the disks on average throughout the volume is 2.7X greater for the six source collimated configuration than the six source overlapping configuration. The six-source collimated configuration uses only the small cone angle ($\theta = \pm 2°$) projections from each source to the object, resulting in full modulation intensity throughout the entire phantom.

3.1.2. Corgi phantom—A sagittal slice through the volume data of the Corgi phantom with the cone beam factor modules is displayed in figure 6 alongside line profiles of the data measured orthogonal to the disk planes. This line profile data was used to calculate the modulation in z (figure 4) for four positions within the scanner FOV (in z) as shown in figure 7.

3.1.3. Noise power spectra—An example of a central slice through the 3D NPS is illustrated in figure 8 for all four configurations to show the null cone. This example captures the NPS in a volume of interest that is between 107.2–126.4 mm in the z-dimension. For the one source configuration, this corresponds to the region between 12 to 14 degrees cone angle. It is displayed in a cropped window to feature the null cone and not the apodization of the ramp filter.

The cone angle was measured from a central slice of the 3D NPS (as shown in figure 8(a)) as the half angle within the null cone. To validate this method, the measured cone angle within the null cone map was compared to the true system cone angle from the geometry of the one source configuration. The measured cone angle and true cone angle were plotted

and found to have a coefficient of determination equal to 0.99 showing that the criterion could correctly identify the null elements within the 3D frequency domain. The fraction of the elements within the 3D NPS that were null was tallied for 17 positions through the z-dimension and are plotted in figure 9.

3.1.4.   Anthropomorphic phantom imaging—A slice through the reconstructed volumes was used to visualize the differences in the hand (figure 10) and knee (figure 11). A sagittal slice is displayed to show that the one source configuration cannot recover the entire FOV (figure 10(a)) while the collimated multisource configuration (figure 10(c)) extends the FOV to capture the full length of the hand. A small region of the hand is selected from the image between 55 to 85 mm from the central ray in the one source system because it is positioned at a large cone angle and the qualitative difference in anatomical details is revealing. These improvements in image quality for the six source collimated configuration are due to both a reduction in the cone beam artifacts (figures 7) and a reduction in scatter contamination (discussed in the following section).

Between the metacarpophalangeal joints there are apparent streak artifacts when the one source configuration was used. Figure 11 shows a coronal slice from the knee phantom data positioned at 80 mm from the central ray to illustrate the difference in contrast to noise between the one source configuration (figure 11(a)) and the collimated six source configuration (figure 11(b)). In both anthropomorphic phantoms, the details within the bone structure are obscured when one source is applied, and they are much sharper when the collimated small cone angle configuration is applied. The visibility of these fine structures can impact the diagnostic quality of CBCT scans for many orthopedic applications, as discussed in the introduction.

3.2.   Monte Carlo simulation results for the CBCT system source configurations

3.2.1.   Primary and scatter contributions to projection images—The SPR simulated at the detector surface for the collimated and overlapping configurations is shown in figure 12. A 2D map of the SPR for the collimated one source configuration and the overlapping one source configuration is shown. A subset of the 2D SPR maps was extracted to quantify the SPR along z (figures 12(c)–(d)) by calculating the mean SPR for all dexels within an ROI (1 cm × 1 cm) centered about the z-locations indicated in the figure. Two sets of ROIs were considered, one at the center of the detector columns 'central' and another at the periphery of the columns 'peripheral' which was set at one quarter of the detector width. The specific z locations of the ROIs were chosen to align with the center of the collimated FOV for each source. The maximum SPR was determined by calculating the 95th percentile of the 2D SPR map (figures 12(a)–(b)) within the shadow of the phantom on the detector. The maximum SPR for the collimated configuration was 0.26 while the maximum SPR for the overlapping configuration was 0.81. The scatter distribution was compared between the overlapping and collimated configurations for source A and source F, shown in figure 13. This plot was created by collecting ROIs (1 cm × 1 cm) on the detector to calculate the mean scatter at each row position.

The summation of simulated scatter distributions for collimated sources A,C,E and the summation of collimated sources B,D,F were also compared for a theoretical multisource configuration which utilizes simultaneously triggered sources (labeled 'ACE collimated' and 'BDF collimated' in figure 13). The collimated multisource configuration theoretically allows for simultaneous source activation as illustrated in figure 2 for two consecutive projection images. This is unique to the multisource collimated geometry because there is no overlap of the primary beam from a subset of sources on the detector. In this configuration, sources A, C, E could theoretically be triggered simultaneously and sources B, D, F could also be triggered simultaneously. However, given that the Doheny scanner used in the present experiments does not have the multisource x-ray tube installed, simultaneous triggering is not possible. In the experimental study (section 3.1), only one source was triggered at a time, and a narrow collimation scheme is used to limit the exposure to a sub volume within the total FOV. In a system that is actually triggered simultaneously, there would be an increase in scatter contamination from adjacent sources (as illustrated in figure 13) that would need to be considered. Simultaneous source triggering is discussed further in section 4.2.

3.2.2. 3D dose distributions—The average and maximum dose (95th percentile) for the four different source configurations were calculated from the Monte Carlo simulation results and detailed in table 1. A sagittal slice through the center of the 3D dose distributions for the different source configurations are shown in figure 14. Each dose map is normalized to the maximum dose and displayed on a scale from 0 to 1 in order to show the relative dose distributions. Line profiles (along z) through the 3D dose distributions are also shown in figure 14. An ROI (1 cm × 1 cm) was averaged across the coronal plane of the volume to calculate the data for the line profiles at the center and periphery (1.5 cm from the edge of the phantom) of the 3D dose distributions. The profiles for the overlapping configurations were plotted on a scale from 0 to 3 mGy per 100 mAs while the collimated configuration was plotted from 0 to 1.5 mGy.

4. Discussion

4.1. Experimental study of CBCT system source configurations

The phantom imaging studies presented in this work demonstrate the image quality improvements and utility of the multisource concept applied to CBCT. The Defrise phantom and the Corgi phantom quantify the variable contrast modulation throughout the scanner FOV, and the null cone in the 3D NPS quantifies the missing frequencies throughout the scanner FOV. Within the FOV of the one source configuration, the farther the position is from the central ray, the more information is lost in both the spatial and frequency domains. The collimated six source configuration shows the most improvement for all three phantom studies when compared to the one source configuration. These two configurations were then used to image the two anthropomorphic phantoms (figures 10 and 11) and demonstrated clear qualitative differences in the contrast with the collimated six source configuration providing significantly improved visibility of fine details. The smaller sub volumes in the collimated geometry contribute to a decrease in the noise caused by scattered photons and also essentially eliminates cone beam artifacts because only small cone angles are used

during the acquisition. One limitation of the study was that the built-in collimation of the x-ray tube prevented the full coverage of the detector for the overlapping geometries. This implies that the volume datasets from the overlapping geometries have inconsistent noise properties throughout the FOV.

4.2. Monte Carlo simulation of CBCT system source configurations

The Monte Carlo simulation results demonstrate the differences in the scatter contributions between the collimated and overlapping geometries. For a full FOV (overlapping geometry), the SPR varies down the length of the detector with a peak at the middle of the polyethylene phantom (figure 12(c)). In the collimated geometry configuration, the SPR remains consistent down the length of the detector (figure 12(d)). The scatter interactions were examined separately from the primary interactions and compared between the overlapping and collimated configurations (figure 13) for the top 'A' and bottom 'F' source positions. The magnitude of the scatter is greatly reduced when comparing the overlapping to the collimated source configurations at the same source positions. When only one source is triggered at a time, the scatter is limited and does not depict the scatter that would occur for simultaneously triggered sources that was discussed as a potential benefit of the multisource collimated geometry (but not physically simulated on the breast CT scanner used in this study). Monte Carlo simulation comparisons with simultaneous triggering of multiple collimated sources are also shown in figure 13 (labeled 'ACE collimated' and 'BDF collimated') demonstrating an increase in scatter contamination in the projection domain from adjacent sources as expected.

Simultaneous triggering of multiple sources in the collimated multi-source configuration would however provide a higher duty cycle and therefore make more efficient use of the scan time and improve angular sampling. The duty cycle refers to the fraction of the time within a complete acquisition that an individual source is active. For example, consider a single source (non-simultaneous) acquisition with six sources and a total of 498 projections acquired in 360 degrees. Each source would be active in only 1/6 or equivalently 83 of the 498 projections. With simultaneous pulsing (three sources at a time) and an odd (A,C,E)/even (B,D,F) synchronization approach, each source would contribute to $\frac{1}{2}$ or equivalently 252 of the 504 projections. Hence the duty cycle would increase from 1/6 (0.17) to $\frac{1}{2}$ (0.5) with an increase of a factor of 3.

The 3D dose distributions show that the maximum dose for all the overlapping configurations (one, three & six) remained relatively constant, but the average dose for the multisource (three & six source) overlapping configurations had increased 25% when compared to the one source configuration. This increase in the average dose can be attributed to the improved coverage of the phantom volume near the bottom of the FOV when multiple sources are used as shown in figure 14(b). There is a four-fold decrease in both the average dose and the maximum dose when comparing the collimated six source configuration and all of the overlapping configurations. These results are as expected since the multisource, collimated geometry makes more efficient use of the x-ray beam by not irradiating the object at large cone angles which effectively mitigates cone beam artifacts and reduces scatter contamination in the projection domain as demonstrated in this study.

While these results are promising there is a need to optimize the system geometry for the multisource collimated configuration in order to minimize hot spots in the dose distributions (shown in figure 14(d)) and reduce total scan times by investigating more complex source and detector synchronization schemes.

Future studies are needed on a tabletop multisource CBCT system which allows for simultaneous source triggering in order to optimize the collimated source configurations for minimizing the scatter contaminations and dose contributions while still making efficient use of the source output and minimizing total scan time. This will be made possible by the ongoing development of multisource x-ray array technology (Boone *et al* 2019), which involves multiple individually addressable cathodes and a single rotating cylindrical anode.

5. Conclusions

Multisource CBCT configurations were physically simulated and evaluated based on image quality in the spatial domain, sampling in the frequency domain, radiation dose, and scatter contributions. The multisource overlapping configurations reduced cone beam artifacts and improved frequency sampling relative to a single source configuration, but the contrast is compromised and there is considerable scatter contribution to the signal. The collimated multisource concept applied to CBCT was shown to significantly reduce scatter (figures 12–13) and improve consistency in image quality (figures 5–7) throughout the FOV when compared to standard CBCT (one source). The collimated beam multisource concept also showed the reduction of artifacts and improvements in contrast in two anthropomorphic phantoms (figures 10–11).

The combination of improved image quality and reduced dose makes the collimated six source configuration for CBCT a promising potential modality for clinical imaging. Therefore, we believe that collimated multisource CBCT applied to clinical applications has the potential to provide more consistent image quality throughout the FOV and more reliable diagnostic information when compared to standard one source CBCT.

Acknowledgments

References

Baek J and Pelc NJ 2010 A new method to combine 3D reconstruction volumes for multiple parallel circular cone beam orbits Med. Phys 37 5351–60 [PubMed: 21089770]

Baek J and Pelc NJ 2011 Local and global 3D noise power spectrum in cone-beam CT system with FDK reconstruction Med. Phys 38 2122–31 [PubMed: 21626945]

Bartolac S, Clackdoyle R, Noo F, Siewerdsen J, Moseley D and Jaffray D 2009 A local shift-variant Fourier model and experimental validation of circular cone-beam computed tomography artifacts Med. Phys 36 500–12 [PubMed: 19291989]

Boone JM, Becker AE, Hernandez AM, Dobbins JT and Schwoebelc P 2019 Multi-x-ray source array for stationary tomosynthesisor multi-cone angle cone beam CT Proc. SPIE 10948 10948OU

Chen Y, Song Y, Ma J and Zhao J 2016 Optimization-based scatter estimation using primary modulation for computed tomography Med. Phys 43 4753–67 [PubMed: 27487893]

Chen Y, Xi Y and Zhao J 2014a A SEMI-stationary CT system 2014 IEEE 11th Int. Symp. on Biomedical Imaging, ISBI 2014 (Institute of Electrical and Electronics Engineers Inc.) pp 1099–102

Chen Y, Xi Y and Zhao J 2014b A stationary computed tomography system with cylindrically distributed sources and detectors J. X-Ray Sci. Technol 22 707–25

Demehri S et al. 2015 Assessment of image quality in soft tissue and bone visualization tasks for a dedicated extremity cone-beam CT system Eur. Radiol 25 1742–51 [PubMed: 25599933]

Endo M, Tsunoo T, Nakamori N and Yoshida K 2001 Effect of scattered radiation on image noise in cone beam CT Med. Phys 28 469–74 [PubMed: 11339743]

Faccioli N, Foti G, Barillari M, Atzei A and Mucelli RP 2010 Finger fractures imaging: accuracy of cone-beam computed tomography and multislice computed tomography Skelet. Radiol 39 1087–95

Fahrig R, Dixon R, Payne T, Morin RL, Ganguly A and Strobel N 2006 Dose and image quality for a cone-beam C-arm CT system Med. Phys 33 4541–50 [PubMed: 17278805]

Feldkamp LA, Davis LC and Kress JW 1984 Practical cone-beam algorithm J. Opt. Soc. Am. A 1 612–9

Fu J and Fan D 2015 Volumetric reconstruction technique for multiple parallel circular orbits CT 2015 Int. Conf. on Mechatronics, Electronic, Industrial and Control Engineering (MEIC-15) (April 2015) (10.2991/meic-15.2015.33)

Gang GJ et al. 2018 Image quality and dose for a multisource cone-beam CT extremity scanner Med. Phys 45 144–55 [PubMed: 29121409]

Gazi PM, Yang K, Burkett GW, Aminololama-Shakeri S, Anthony Seibert J and Boone JM 2015 Evolution of spatial resolution in breast CT at UC Davis Med. Phys 42 1973–81 [PubMed: 25832088]

Ghazi P, Hernandez AM, Abbey C, Yang K and Boone JM 2019 Shading artifact correction in breast CT using an interleaved deep learning segmentation and maximum likelihood polynomial fitting approach Med. Phys 46 mp.13599

Gilat Schmidt T. 2009; Preliminary feasibility of dedicated breast CT with an inverse geometry. Proc. SPIE. 7258 :72582Y.

Gong H, Li B, Jia X and Cao G 2018 Physics model-based scatter correction in multi-source interior computed tomography IEEE Trans. Med. Imaging 37 349–60 [PubMed: 28829306]

Han C and Baek J 2019 Multi-pass approach to reduce cone-beam artifacts in a circular orbit cone-beam CT system Opt. Express 27 10108 [PubMed: 31045157]

Hernandez AM and Boone JM 2014 Tungsten anode spectral model using interpolating cubic splines: unfiltered x-ray spectra from 20 kV to 640 kV Med. Phys 41 042101 [PubMed: 24694149]

Jaffray D, Siewerdsen J and Gospodarowicz M 2008 Radiation oncology Image-Guided Interventions (Boston, MA: Springer US) pp 501–29

Jaffray DA, Siewerdsen JH, Wong JW and Martinez AA 2002 Flat-panel cone-beam computed tomography for image-guided radiation therapy Int. J. Radiat. Oncol 53 1337–49

Kachelrieß M, Knaup M and Kalender WA 2006 Multithreaded cardiac CT Med. Phys 33 2435–47 [PubMed: 16898446]

Lindfors KK, Boone JM, Nelson TR, Yang K, Kwan ALC and Miller DF 2008 Dedicated breast CT: initial clinical experience Radiology 246 725–33 [PubMed: 18195383]

MCNP X 2003 Monte Carlo team, MCNP—a general purpose Monte Carlo N-particle transport code, version 5. LA-UR-03–1987 (Los Alamos National Laboratory)

Miracle AC and Mukherji SK 2009 Conebeam CT of the head and neck, part 2: clinical applications Am. J. Neuroradiol 30 1285–92 [PubMed: 19461061]

Neculaes VB et al. 2016 Multisource inverse-geometry CT. Part II. X-ray source design and prototype Med. Phys 43 4617–27 [PubMed: 27487878]

Neubauer J. et al. 2016; Comparison of diagnostic accuracy of radiation dose-equivalent radiography, multidetector computed tomography and cone beam computed tomography for fractures of adult cadaveric wrists. PloS One. 11 :e0164859. [PubMed: 27788215]

Ozaki Y, Watanabe H, Nomura Y, Honda E, Sumi Y and Kurabayashi T 2013 Location dependency of the spatial resolution of cone beam computed tomograph for dental use Oral Surg. Oral Med. Oral Pathol. Oral Radiol 116 648–55

Parsa A, Ibrahim N, Hassan B, van der Stelt P and Wismeijer D 2015 Bone quality evaluation at dental implant site using multislice CT, micro-CT, and cone beam CT Clin. Oral Implants Res 26 e1–e7

Poludniowski G, Evans PM, Hansen VN and Webb S 2009 An efficient Monte Carlo-based algorithm for scatter correction in keV cone-beam CT Phys. Med. Biol 54 3847–64 [PubMed: 19491449]

Posadzy M, Desimpel J and Vanhoenacker F 2018 Cone beam CT of the musculoskeletal system: clinical applications Insights Imaging 9 35–45 [PubMed: 29302798]

Robb RA 1982 The dynamic spatial reconstructor: an x-ray video-fluoroscopic CT scanner for dynamic volume imaging of moving organs IEEE Trans. Med. Imaging 1 22–33 [PubMed: 18238255]

Scarfe WC and Farman AG 2008 What is cone-beam CT and how does it work? Dent. Clin. North Am 52 707–30 [PubMed: 18805225]

Schmidt TG, Fahrig R, Pelc NJ and Solomon EG 2004 An inverse-geometry volumetric CT system with a large-area scanned source: a feasibility study Med. Phys 31 2623–7 [PubMed: 15487745]

Shah JP, Mann SD, Mckinley RL and Tornai MP 2015 Three dimensional dose distribution comparison of simple and complex acquisition trajectories in dedicated breast CT Med. Phys 42 4497–510 [PubMed: 26233179]

Siewerdsen JH et al. 2005 A simple, direct method for x-ray scatter estimation and correction in digital radiography and cone-beam CT Med. Phys 33 187–97

Siewerdsen JH, Moseley DJ, Bakhtiar B, Richard S and Jaffray DA 2004 The influence of antiscatter grids on soft-tissue detectability in cone-beam computed tomography with flat-panel detectors Med. Phys 31 3506–20 [PubMed: 15651634]

Siewerdsen JH et al. 2019 Cone-beam CT dose and imaging performance evaluation 5 with a modular, multi-purpose phantom Med. Phys 47 467–79 [PubMed: 31808950]

Smans K et al. 2010 Simulation of image detectors in radiology for determination of scatter-to-primary ratios using Monte Carlo radiation transport code MCNP/MCNPX Med. Phys 37 2082–91 [PubMed: 20527541]

Tuy HK 1983 An inversion formula for cone-beam reconstruction SIAM J. Appl. Math 43 546–52

Vedantham S, Shi L, Karellas A and Noo F 2012 Dedicated breast CT: radiation dose for circle-plus-line trajectory Med. Phys 39 1530–41 [PubMed: 22380385]

Wood R et al. 2013 Factors affecting the accuracy of buccal alveolar bone height measurements from cone-beam computed tomography images Am. J. Orthod. Dentofac. Orthop 143 353–63

Yoo S and Yin -F-F 2006 Dosimetric feasibility of cone-beam CT-based treatment planning compared to CT-based treatment planning Int. J. Radiat. Oncol. Biol. Phys 66 1553–61 [PubMed: 17056197]

Zhao J, Jin Y, Lu Y and Wang G 2009 A filtered backprojection algorithm for triple-source helical cone-beam CT IEEE Trans. Med. Imaging 28 384–93 [PubMed: 19244010]

Zhu L, Xie Y, Wang J and Xing L 2009 Scatter correction for cone-beam CT in radiation therapy Med. Phys 36 2258–68 [PubMed: 19610315]

Zhye Y and De Man Bruno PJ 2009 3D analytic cone-beam reconstruction for multiaxial CT acquisitions Int. J. Biomed. Imaging 2009 1–11
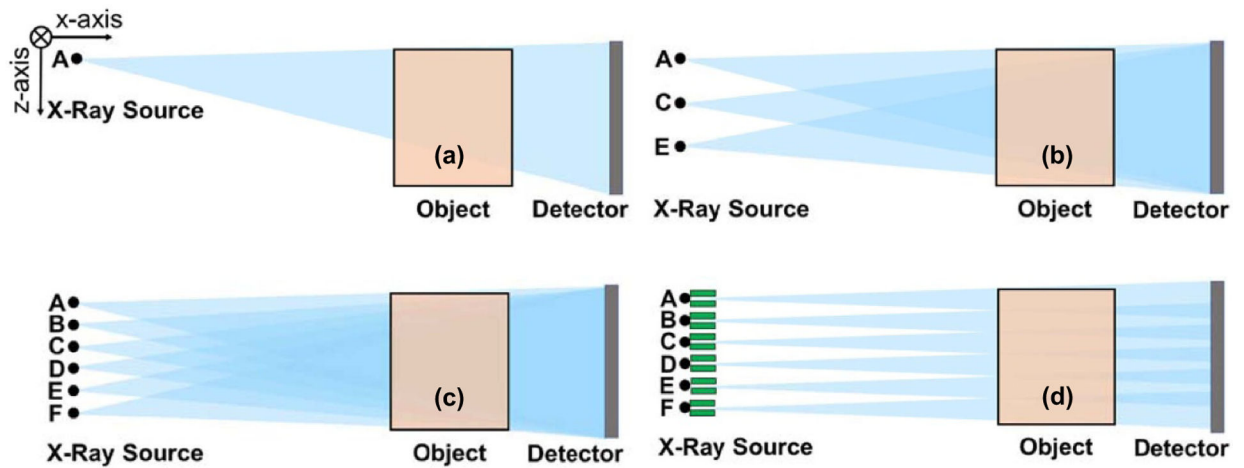
Figure 1.
Diagrams of the geometry of each CBCT system: (a) one source, (b) three source overlapping, (c) six source overlapping, (d) six source collimated configuration. The narrow collimators are indicated in green. The blue indicates the spatial distribution of the x-ray beams. The position of each source location is constant across the different geometries. The diagrams are drawn to relative scale for a source to isocenter distance of 500 mm, source to detector distance of 700 mm, detector height of 200 mm, sources separated by 30 mm in the z-dimension, and an object space of $153.6 \times 153.6 \times 180$ mm.
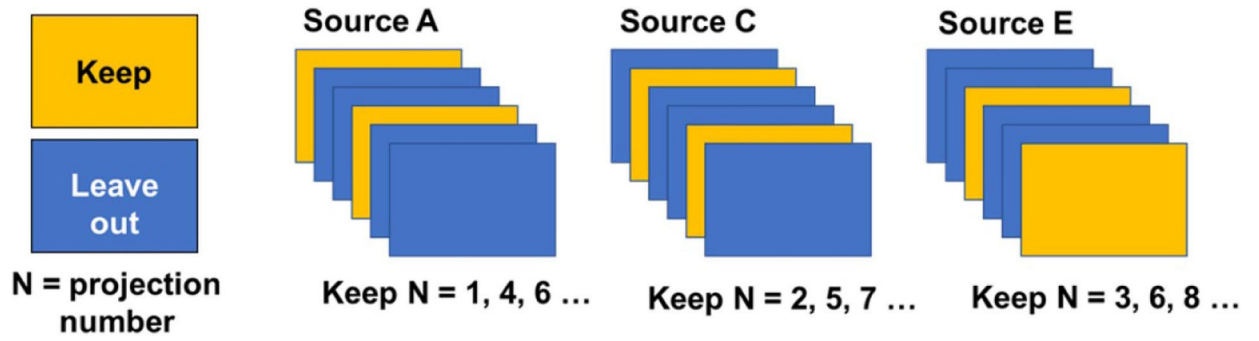
Figure 2.
Diagram detailing the method used for image reconstruction for the overlapping multisource configurations which involves selecting a subset of each full acquisition to interleave into a combined reconstruction. An example for the overlapping three source configuration is shown.
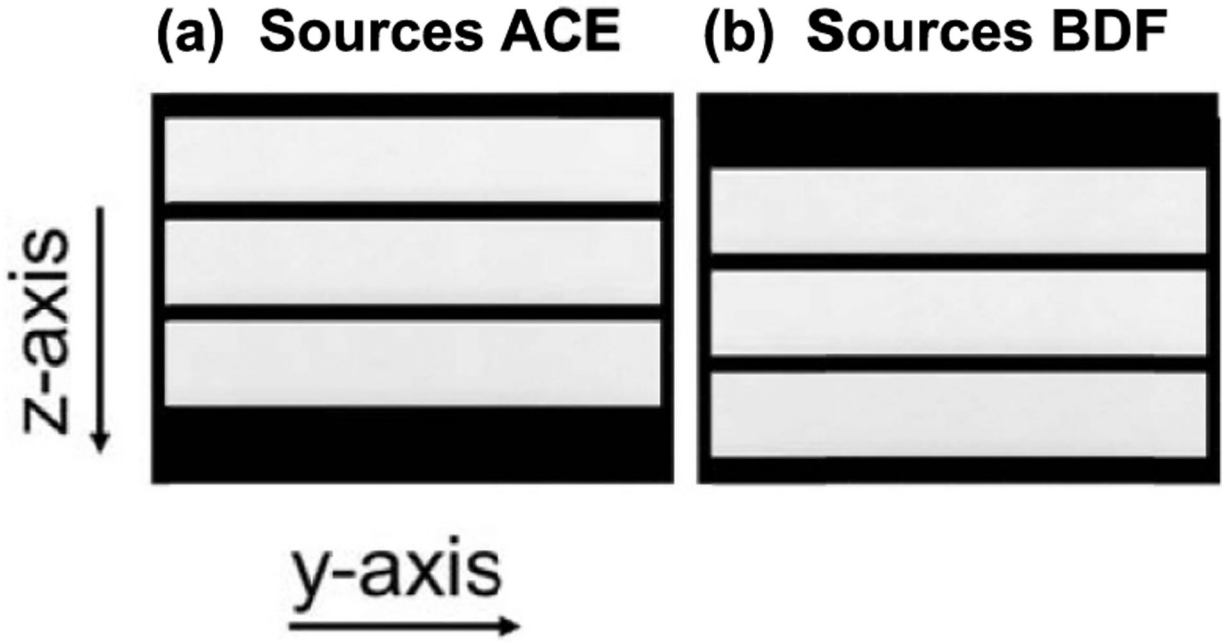
Figure 3.
The detector (Varex Dexela 2923 CMOS) coverage applied for the collimated six source geometry, (a) Coverage for sources A, C, E digitally combined, (b) coverage for sources B, D, F digitally combined. Each source covers 330 rows which equates to 49.5 mm on the detector and a 2-degree cone angle both posteriorly and anteriorly.
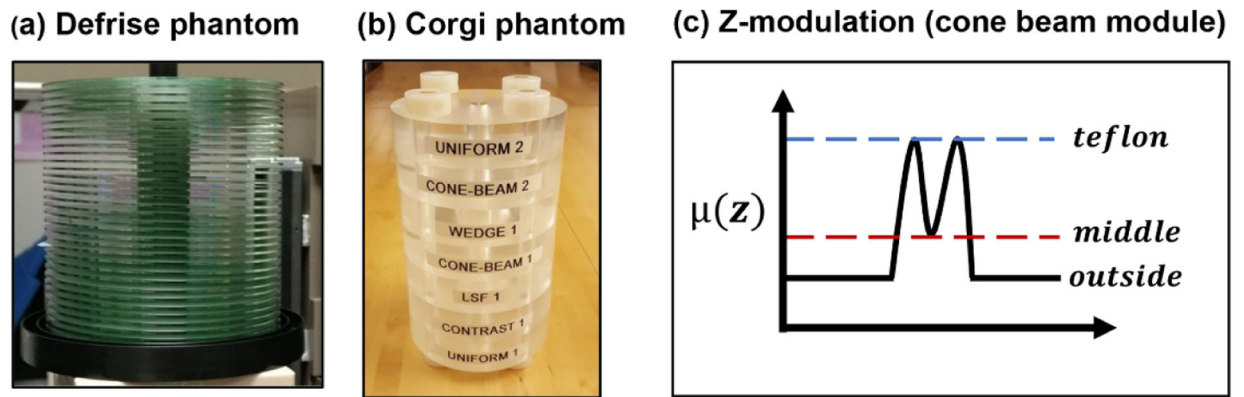
Figure 4.
Photos of the (a) Defrise phantom and the (b) Corgi phantom used in the quantitative experimental study. (c) Line pair demonstration to show the calculation of the loss in modulation in the z-dimension (z_{mod}) through the volume data set of the Corgi phantom cone beam artifact module.
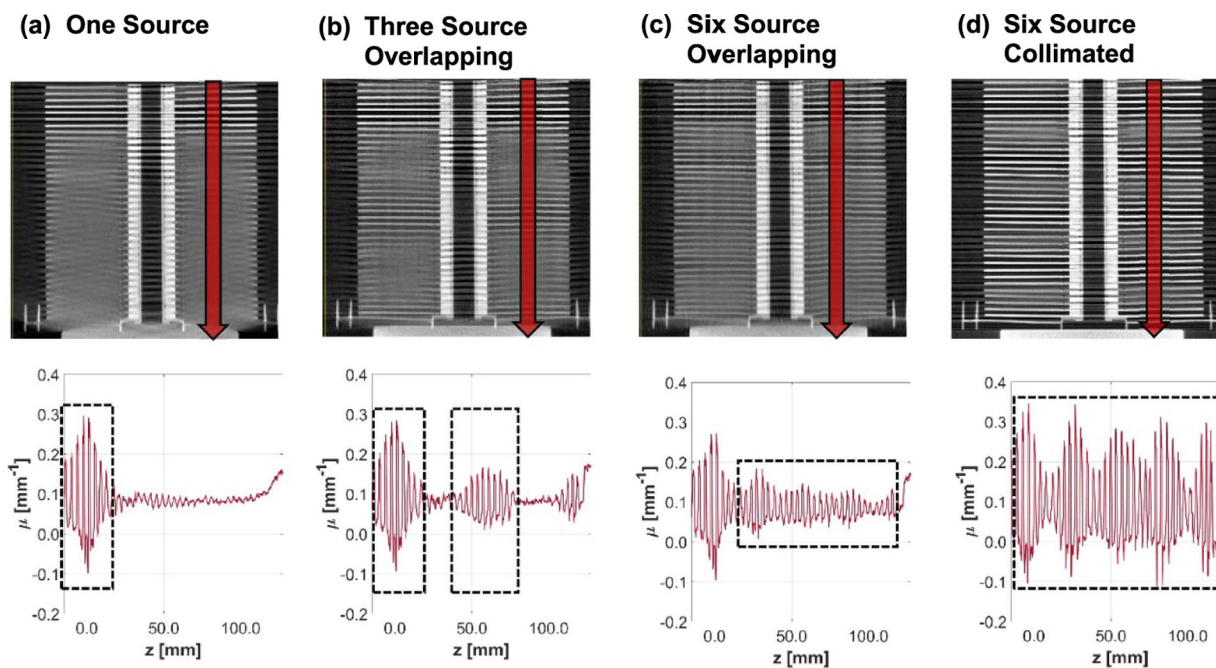
Figure 5.
Defrise phantom results are shown for the (a) one source, (b) three source overlapping, (c) six source overlapping, and (d) six source collimated configurations. Sagittal slices through the reconstructions are shown in the top row qualitatively demonstrating modulation of the disks and the bottom row shows line plots through the volume quantifying the modulation.

(a) One Source

(b) Six Source Overlapping

(c) Six Source Collimated
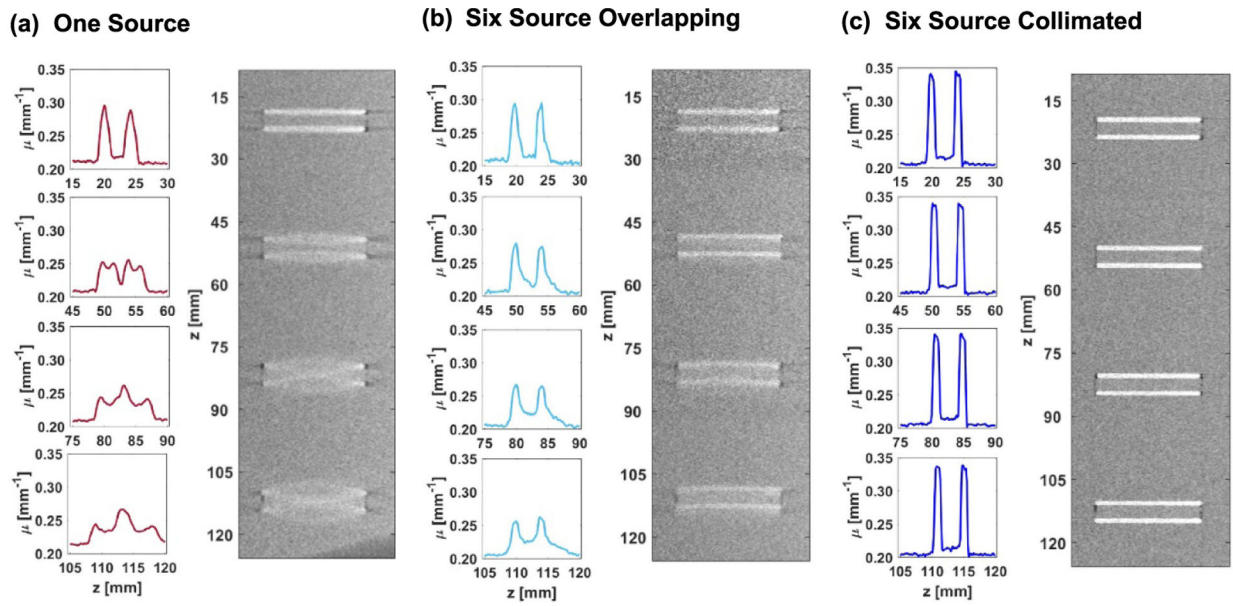
Figure 6.
Cone beam modules from the Corgi phantom used to evaluate the modulation in z at various vertical locations throughout the object space. Each row of data corresponds to a position in the z-dimension relative to the central ray displayed on the right.
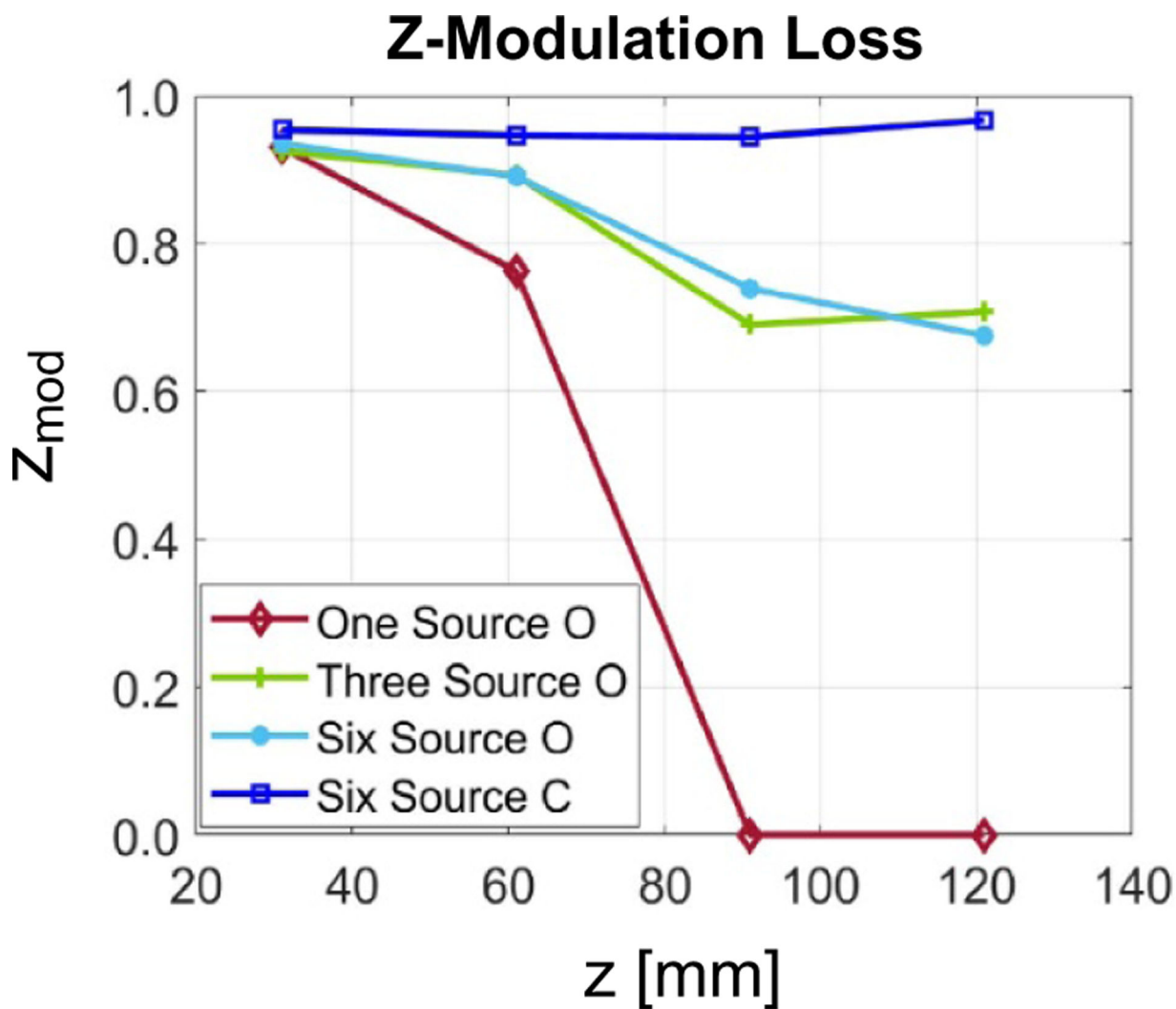
Figure 7.
Cone beam artifact measured as the loss in modulation in the *z*-dimension for several multisource systems compared to the one source system for four locations along the *z*-dimension relative to the central ray. Four configurations are represented: one source, three source overlapping, six source overlapping, six source collimated. In the legend, O = overlapping and C = collimated.
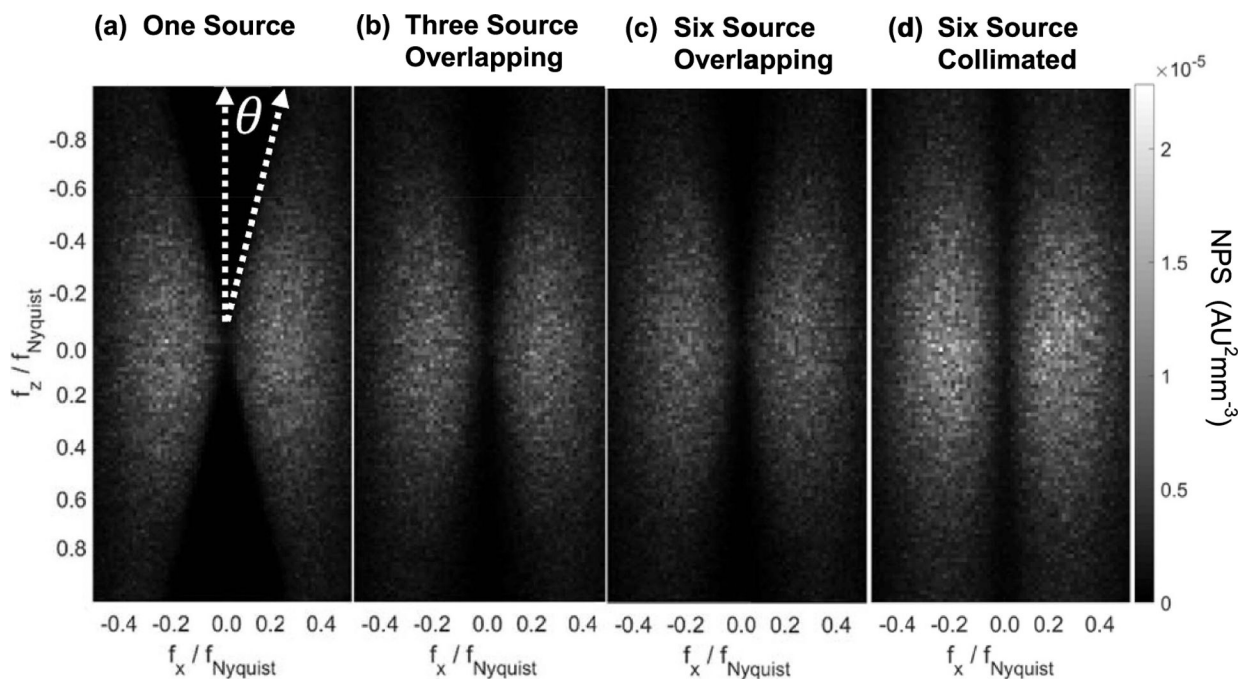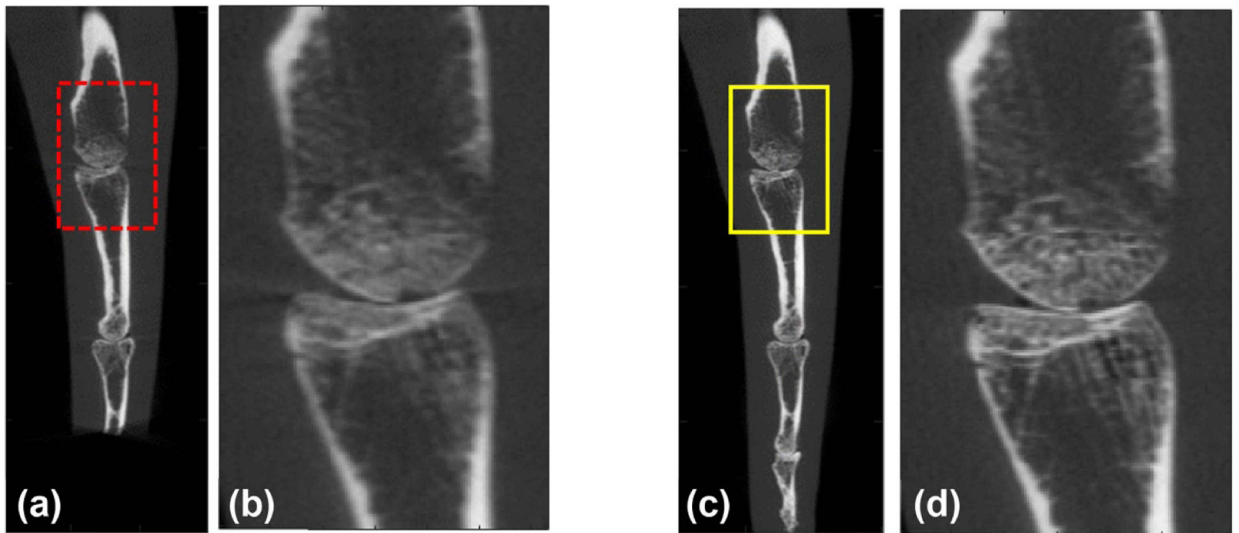
Figure 8.
Sagittal slices though the 3D NPS for the four different MXA configurations at a cone angle of 14 degrees (relative to one source) to illustrate the null cone recovery in the multisource systems. (a) One source configuration with an illustration of the null cone measurement, (b) three source overlaped configuration, (c) six source overlapping configuration, (d) six source collimated configuration.
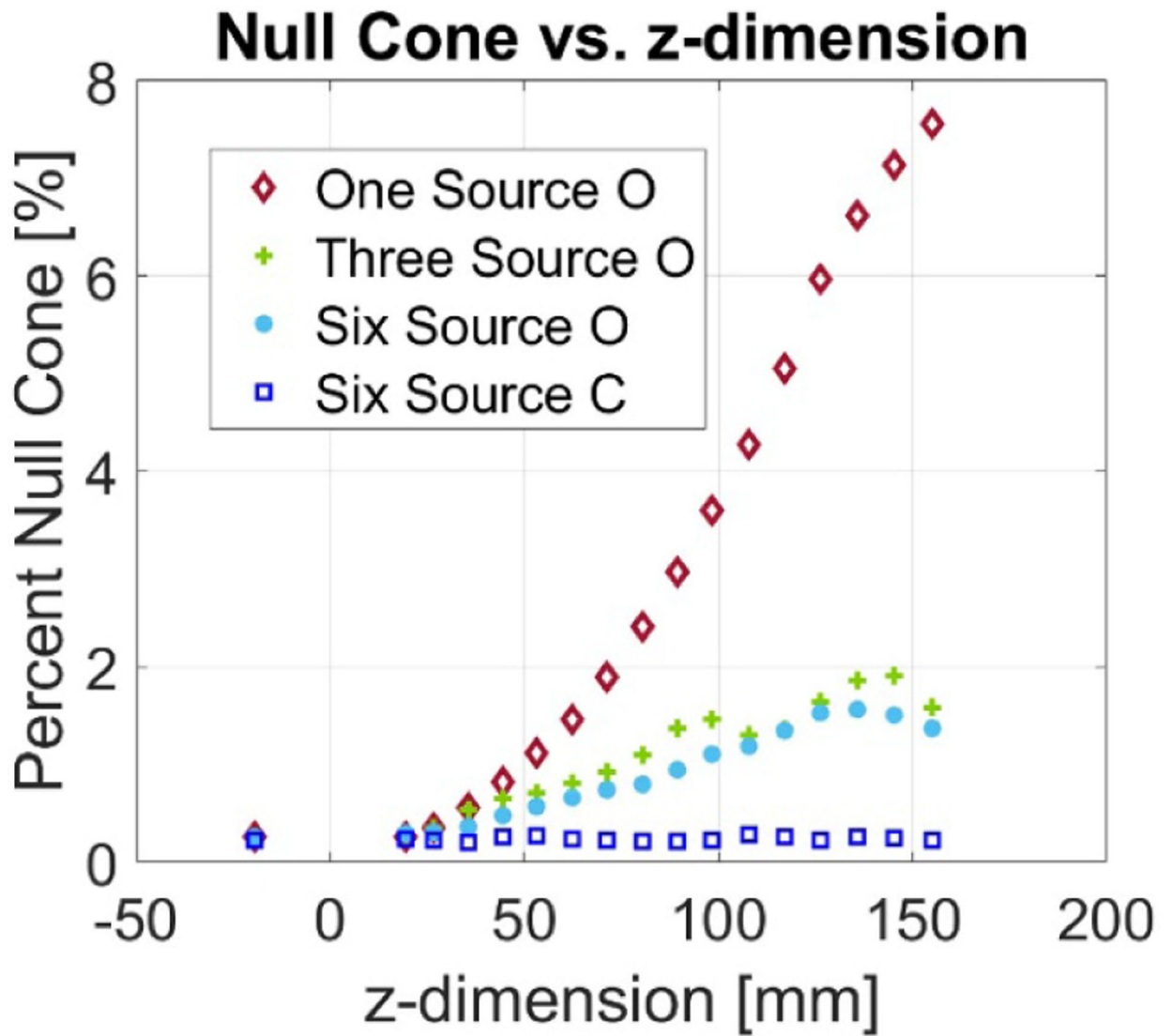
Figure 9.
Percent null cone within the 3D NPS plotted at 16 locations through the field of view. Four configurations are represented: one source, three source overlapping, six source overlapping, six source collimated. In the legend, O = overlapping and C = collimated.

Figure 10.
Anthropomorphic hand phantom scanned by both the one source system and the collimated six source system. Sagittal slices are shown through the reconstructed volumes with a region of interest. (a) One source system full FOV, (b) one source system ROI FOV, (c) six source collimated configuration full FOV, (d) six source collimated configuration ROI FOV. The slices were displayed with the same window range [0, 1.2] to make a fair comparison.
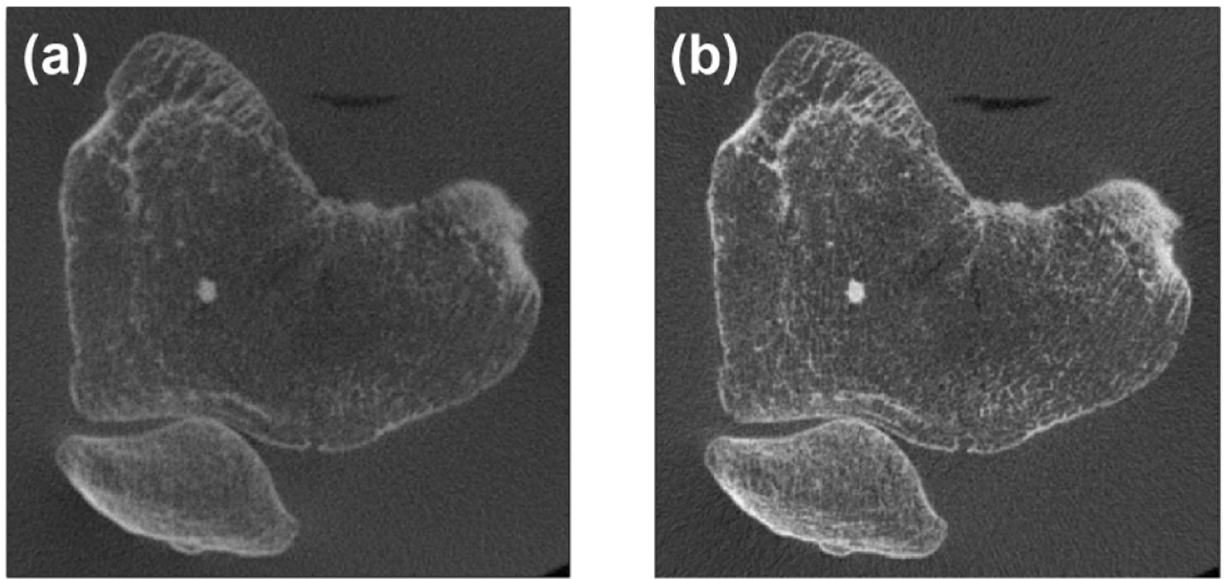
Figure 11.
Anthropomorphic knee phantom scanned by both the one source system and the collimated six source system. Coronal slices are shown through the reconstructed volumes at 80 mm from the central ray, which corresponds to a cone angle of 9° in the one source configuration. (a) One source configuration, (b) collimated six source configuration. The slices are displayed with the same window range [0, 0.9] to make a fair comparison.
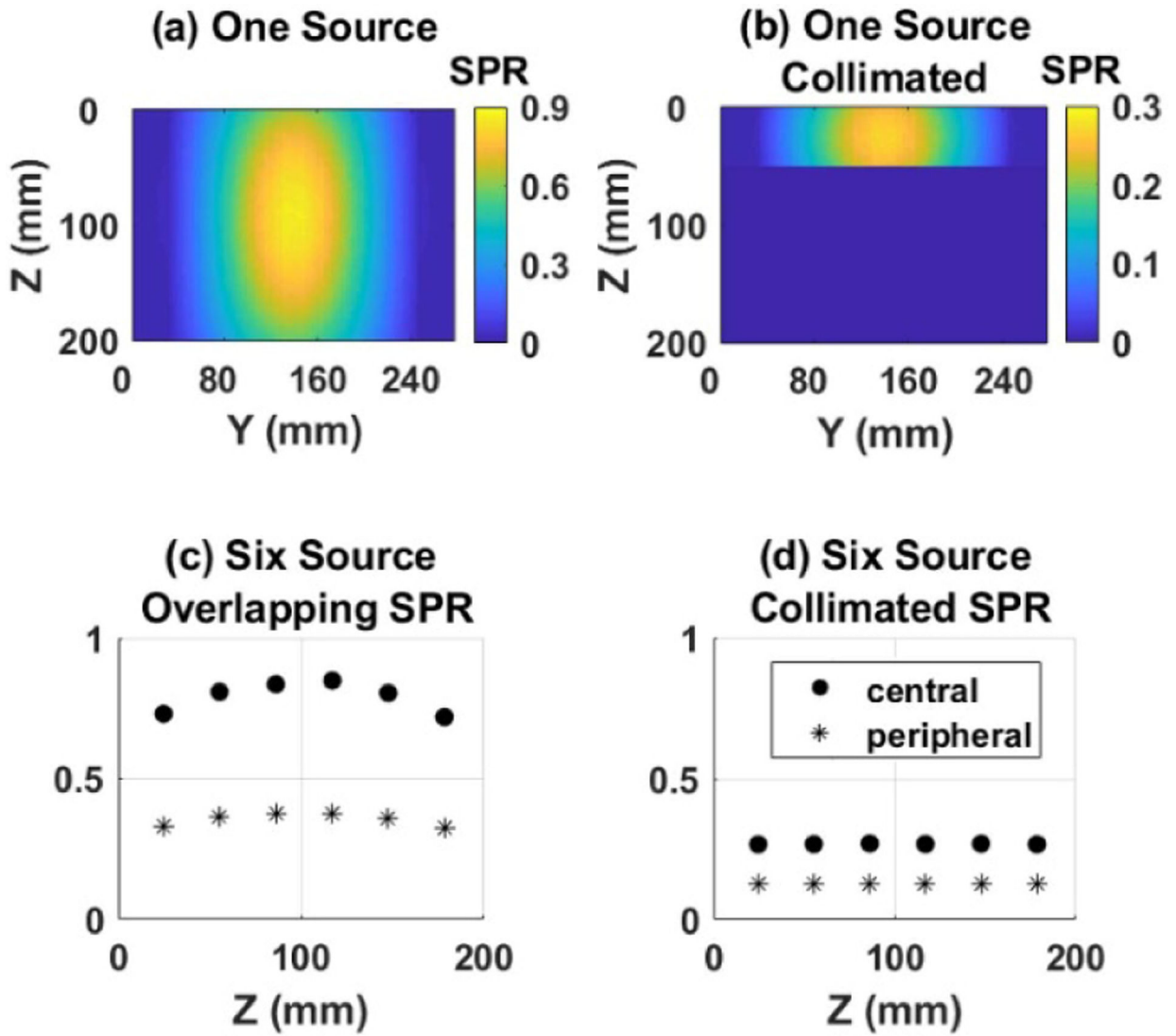
Figure 12.
Top row: Monte Carlo simulation results showing 2D maps of the scatter to primary ratio (SPR) on the detector surface for a 154.2 mm polyethylene cylinder scanned using one source position 'A' in the (a) overlapping configuration and the (b) collimated configuration. Bottom row: 1D SPR profiles along the z (rows) of the simulated detector in the (c) six source overlapping configuration and the (d) six source collimated configuration are also shown. The central ROIs were centered about $y = 139$ mm and peripheral ROIs were centered about $y = 69$ mm. Along the z dimension, the ROIs (central & periphery) were centered about $z = 25, 55, 85, 115, 145,$ and 175 mm.
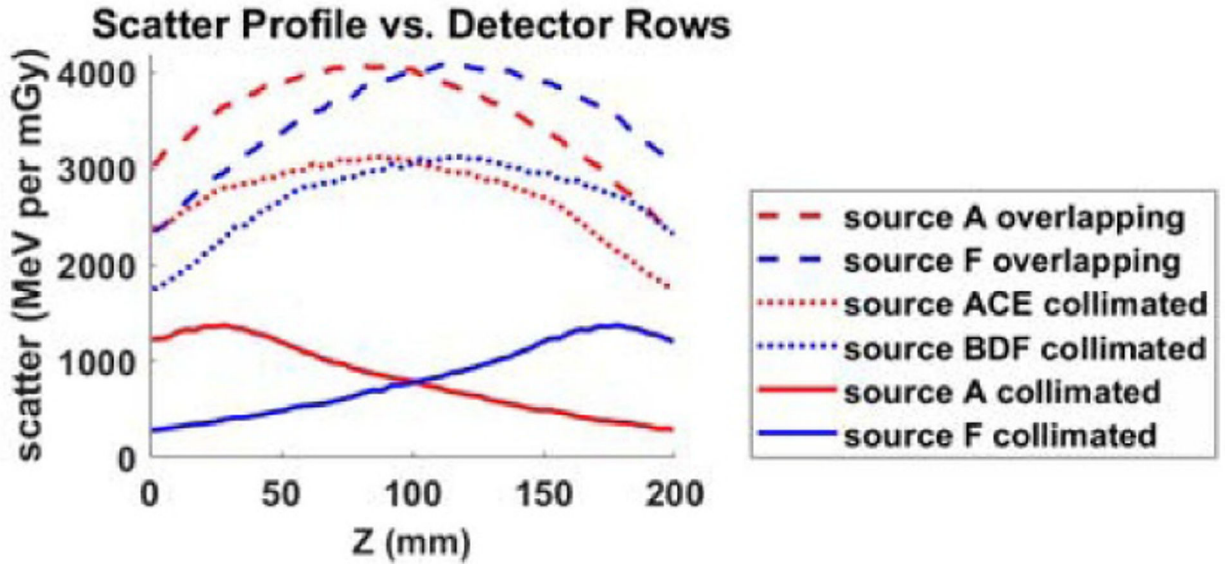
Figure 13.
Line profile down the detector rows at the center of the columns Y(mm) = 139 to show the magnitude of the scatter distribution for source A and source F in both the collimated and overlapping configurations. The simulated air kerma (mGy per source particle) was used to normalize the projection images (MeV per source particle) to calculate the scatter (MeV per mGy) plotted here.
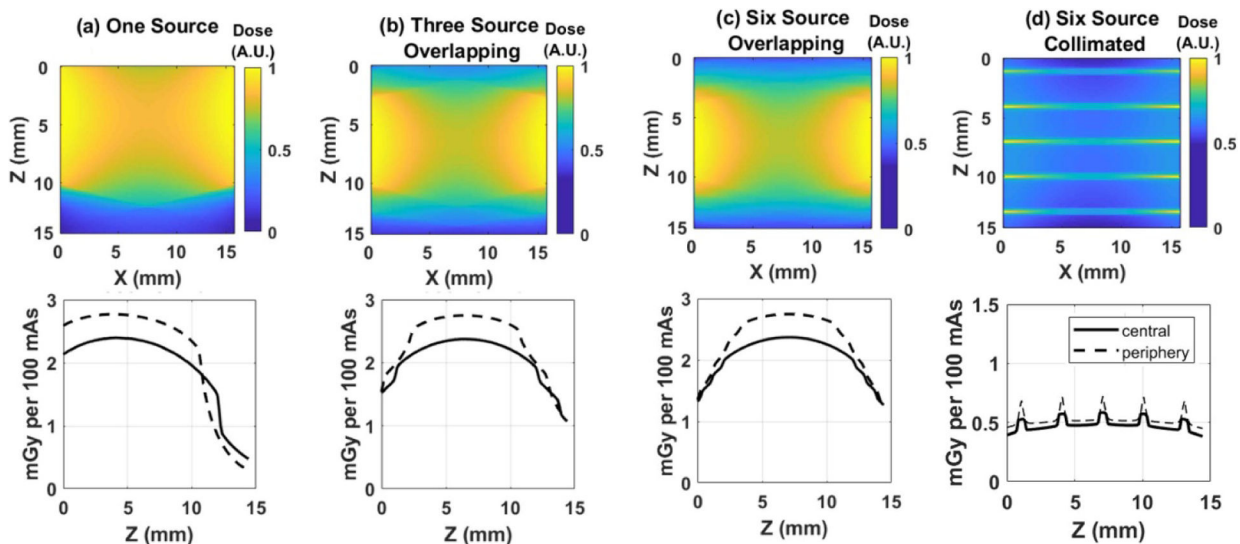
Figure 14.

Top row: central slices through the 3D dose distributions for the various multisource configurations, each normalized to the maximum dose within the corresponding volume. Bottom row: line profiles through the 3D dose distributions at the center and periphery of the volume.

Table 1.

Monte Carlo dosimetry metrics for the various multisource CBCT configurations.

Metric	One source	Three source overlapping	Six source overlapping	Six source collimated
Number of projections per source	498	166	83	498
Dose, average (mGy/100 mAs)	2.098	2.256	2.259	0.513
Dose, maximum (mGy/100 mAs)	2.864	2.827	2.823	0.640